RESEARCH ARTICLE | DECEMBER 05 2024

Modeling of the brain movement and cerebrospinal fluid flow within porous subarachnoid space under translational impacts

Ji Lang (郎骥) ; Qianhong Wu (吴千红)

Physics of Fluids 36, 121908 (2024)
https://doi.org/10.1063/5.0239210

Physics of Fluids ARTICLE pubs.aip.org/aip/pof

Modeling of the brain movement and cerebrospinal fluid flow within porous subarachnoid space under translational impacts

Cite as: Phys. Fluids **36**, 121908 (2024); doi: 10.1063/5.0239210
Submitted: 18 September 2024 · Accepted: 11 November 2024 ·
Published Online: 5 December 2024

Ji Lang (郎骥)[1] and Qianhong Wu (吴千红)[2,3,a)]

AFFILIATIONS

[1]Jiangsu Key Laboratory for Design and Manufacture of Micro-Nano Biomedical Instruments, School of Mechanical Engineering, Southeast University, Nanjing 211189, China
[2]Cellular Biomechanics and Sports Science Laboratory, Villanova University, 800 E Lancaster Avenue, Villanova, Pennsylvania 19085, USA
[3]Department of Mechanical Engineering, Villanova University, 800 E Lancaster Avenue, Villanova, Pennsylvania 19085, USA

[a)]**Author to whom correspondences should be addressed:** qianhong.wu@villanova.edu

ABSTRACT

Traumatic brain injury remains a significant global health concern, requiring advanced understanding and mitigation strategies. In current brain concussion research, there is a significant knowledge gap: the critical role of transient cerebrospinal fluid (CSF) flow in the porous subarachnoid space (SAS) has long been overlooked. To address this limitation, we are developing a simplified mathematical model to investigate the CSF pressurization in the porous arachnoid trabeculae and the resulting motion of brain matter when the head is exposed to a translational impact. The model simplifies the head into an inner solid object (brain) and an outer rigid shell (skull) with a thin, porous fluid gap (SAS). The CSF flow in the impact side (coup region) and the opposite side (contrecoup region) is modeled as porous squeezing and expanding flows, respectively. The flow through the side regions, which connect these regions, is governed by Darcy's law. We found that the porous arachnoid trabeculae network significantly dampens brain motion and reduces pressure variations within the SAS compared to a SAS without the porous arachnoid trabeculae (AT). This effect is particularly pronounced under high-frequency, periodic acceleration impacts, thereby lowering the risk of injury. The dampening effect can be attributed to the low permeability of the AT, which increases resistance to fluid movement and stabilizes the fluid and pressure responses within the SAS, thereby reducing extreme pressure fluctuations and brain displacement under impact. This work provides a foundational understanding of CSF flow dynamics, paving the way for innovative approaches to brain injury prevention and management.

I. INTRODUCTION

Impacts on the head are the leading cause of traumatic brain injury (TBI),[1–3] which remains a significant global health concern, exerting profound effects on both individual well-being and economic stability.[4,5] Annually, about 1.6 to 2.8 million TBIs occur worldwide due to sporting activities alone.[6–8] The severity of TBI varies, ranging from mild to moderate or severe, with more than 75% of cases classified as mild.[9,10] However, even mild TBI can cause symptoms, including cognitive impairments, behavioral disruptions, headaches, and visual disturbances, which significantly impede patients from engaging in work, social interactions, and routine activities.[11,12]

Despite their high prevalence, the mechanical and biological mechanisms underlying brain injuries are still not fully understood. Figure 1 illustrates the structure of the human head, which includes the skull on the outside, brain matter at the center, and the subarachnoid space (SAS) in between, with SAS's average thickness being approximately 3 mm.[13] The SAS and the ventricle spaces are filled with cerebrospinal fluid (CSF), allowing the brain to float within the cranial cavity.[14,15] During the impact process, the gap size of the SAS changes abruptly, causing significant pressure variations within the SAS. In contrast, the size of the ventricles remains relatively unchanged due to the impact, resulting in minimal pressure fluctuations within the ventricles. Importantly, as shown in Fig. 1, the SAS contains

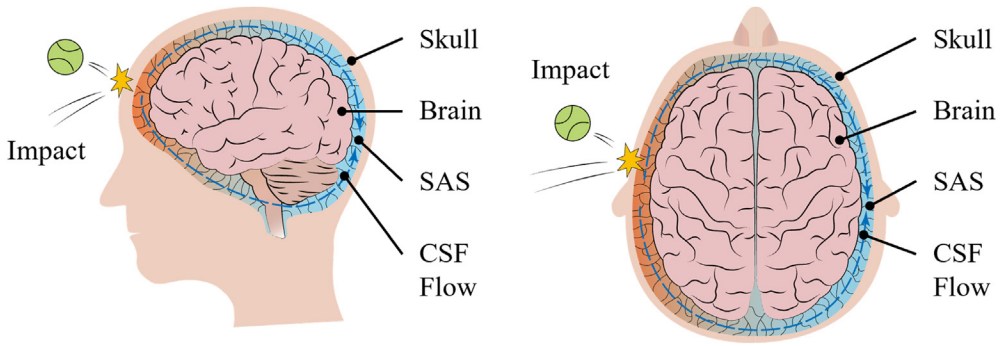

FIG. 1. Schematic diagram of the head. The head consists of a rigid skull on the outside, soft brain matter in the center, and SAS in between. The SAS contains fibrous AT and is filled with CSF. Impacts on the head can induce relative brain motion and corresponding CSF flow within the SAS.

delicate connective tissue strands, with Young's modulus ranging from 1 kPa to approximately 10 kPa,[16,17] named arachnoid trabeculae (AT).[13,18–20] These flexible strands connect the inner surface of the skull to the outer surface of the brain matter. To prevent TBI and related disorders, it is critical to understand the motion of the brain matter bathed in the CSF when the head is exposed to sudden external impacts. State-of-the-art computational and experimental research has been conducted to understand brain injuries. Postmortem[21] and animal studies[22] have focused on the long-term effects of brain injury. Physical models using head surrogates have been crafted to recreate the brain's response to external impacts.[23–25] Numerical simulations using finite element analysis have been developed to examine localized brain tissue damage, treating brain matter and the CSF as inhomogeneous, viscoelastic, or hyperplastic material.[26,27] The physiological roles of CSF flow in brain health maintenance under normal activities, on a timescale of hours to days, have been extensively studied.[28] However, no study has examined the transient CSF flow through the porous SAS within a time frame from milliseconds to seconds during brain concussion.

When the head is exposed to sudden translational impacts, the CSF in the SAS is expected to be squeezed out locally, as shown in Fig. 1. This is a classical fluid mechanics problem known as squeezing flow. Extensive research has investigated the squeezing flow phenomenon, highlighting its excellent damping effect.[29] Squeezing flow problems are complicated due to the interplay between inertial effects and viscous forces resulting from boundary movement.[30,31] Stefan's pioneering work introduced a quasi-static model for squeezing flow, which examines how pressure builds up in a fluid gap confined between two moving boundaries.[32] In this model, inertial effects have been neglected and pressure responses are directly linked to the gap thickness between the boundaries and their relative velocity. This framework has since become a foundational approach for understanding fluid pressurization in confined spaces.[33–36] As research in squeezing flow progresses, the significance of inertial effects has gained recognition.[37–40] Inertial effects are consistently present, as squeezing flow never truly reaches a steady state. The inertia effect is particularly notable when the boundary undergoes significant acceleration, potentially surpassing the pressure response caused by viscosity.[29,41] Consequently, similarity approaches[42–44] and perturbation methods[45,46] have been developed to incorporate both inertial and viscous effects. In the context of brain concussion, the characteristic parameters are as follows: the gap thickness, h, is on the order of 10^{-3} m, and the characteristic collapse time under a constant force typically exceeds 10 seconds, leading to an average velocity, U, on the order of 10^{-4} m /s. The kinetic viscosity ν of CSF is approximately 10^{-6} m^2/s. With these values, the Reynolds number $\mathrm{Re} = Uh/\nu$ is in around of 10^{-1}, indicating minimal convective effects. Additionally, since the impact force duration, t_p, is usually less than 0.1 second, the Strouhal number $\mathrm{Sr} = t_p U/h$ is approximately 10^{-2}, indicating that the local acceleration remains significant. This highly transient feature of the CSF flow was examined theoretically[29] and experimentally[41] by our group, focusing on localized squeezing flow dynamics, which lays the foundation for the first analytical model to examine the motion of brain matter as a result of CSF flow and pressurization.[47]

As shown in Fig. 1, translational impacts create a pressure gradient within the SAS, promoting relative brain motion within the skull and corresponding CSF flow.[48,49] This movement can initiate a transient squeezing flow in the coup region and an expanding flow in the contrecoup region of the thin SAS space,[50] thereby increasing the magnitude of both positive and negative pressure responses. Negative pressure in the contrecoup region may reach the cavitation threshold, approximately equal to the vaporization pressure of CSF (around 2 kPa at body temperature), potentially leading to cavitation within the SAS and significantly damaging brain tissue.[23] In our recent study,[47] we developed the first analytical model to describe the motion of brain matter resulting from the squeezing flow at the impact site and a reverse squeezing flow or expanding flow at the contrecoup region, as a constant impact acceleration is imposed on the head. The model offers critical insights into the fundamental mechanisms of brain concussion.[47] However, it did not take into account the critical role of the porous AT network in transmitting and mitigating the impact.

The SAS is filled with the highly porous, fibrous AT network, acting as a protective layer surrounding the brain, adding additional complexity to the squeezing flow within the SAS.[13,50,51] Over the past decade, significant progress has been made in understanding porous media flow, indicating tremendous pore pressure generation when a soft porous medium is suddenly compressed.[52–62] For flow through highly porous structures, Darcy's pioneering work established the relationship between pressure gradient and porous resistance,[63–65] though it excluded viscous and inertial effects, which become significant near solid boundaries or under time-dependent conditions.[66] Additionally, the volume averaging technique has been developed to include both

local and convective accelerations in the governing equations.[67,68] This approach enables a more comprehensive inclusion of viscous and inertial effects in modeling flow through porous media.

The fundamental physics behind this process is that when the porous media is rapidly compressed, there is a marked increase in the hydrodynamic resistance that the transiently trapped fluid encounters as it escapes from the confining boundaries. The increase in the pore pressure scales as $\mathrm{Br}^2 = h^2/K_p$, where Br is the Brinkman number, h is the layer thickness, and K_p is the Darcy permeability. For AT, K_p can be as low as 3.125×10^{-10} m^2 for SAS with $h = 3$ mm.[13] Thus, $\mathrm{Br} = 170$, and the pore pressure generated inside the SAS is expected to be $\mathrm{Br}^2 = 2.89 \times 10^4$ larger than the case of a pure fluid gap lacking an AT network.[57] Our recent study has shown that very small compression of a soft porous media, such as the AT, could lead to a very sharp decrease in the Darcy permeability.[69,70] Hence, the fluid pressurization is even higher. We believe that when the head is exposed to external impacts, the CSF transmits the impact from the skull to the brain matter, while the pore pressure provides tremendous damping protection. Despite its importance in transmitting and mitigating impacts on the head, the porous AT has never been included in brain biomechanics modeling.

A literature review suggests that existing brain biomechanics studies have neglected either CSF, AT, or both, thus failing to accurately replicate the brain's response in real-life scenarios. This significant knowledge gap leads us to explore, in the current paper, the critical role of transient CSF flow in the porous SAS as our head is exposed to sudden external impacts. We will analytically predict the flow of CSF and its pressure distribution throughout the SAS. Additionally, the motion of inner brain matter will be integrated into the analysis to examine factors influencing fluid–solid interactions within the skull.

II. METHODS

The key features of the response in the intracranial space include a rigid shell on the outside, a solid object at the center, and a thin, porous liquid layer in between. Consequently, the theoretical model developed herein simplifies the geometry while preserving these essential characteristics. As shown in Fig. 2, the skull is modeled as a rigid cylindrical shell on the outside, and the brain is represented as a smaller solid cylinder at the center. The gap in between is modeled as a porous fluid gap with a small gap thickness, creating a liquid environment for the inner solid object. The rigid shell is assumed to receive external impacts and move with acceleration G.

This idealized cylindrical model is chosen to retain the essential structural features of the head—the rigid outer shell, central solid core, and thin, porous fluid layer representing the SAS—while enabling a more tractable theoretical analysis of fluid–structure interactions within the intracranial space. By simplifying the head's geometry to a cylindrical form, the model can capture the primary mechanisms of CSF pressurization and brain motion under impact conditions, allowing us to focus on the dynamic response within the SAS.

This model is designed to simulate concussive events characterized by rapid translational impacts with a relatively large contact area, particularly when the impact is directed at central anatomical locations, such as the forehead or occipital regions. These conditions typically produce uniform, high-frequency accelerations, which are consistent with the model's assumptions of global brain motion and pressure variations within the SAS.

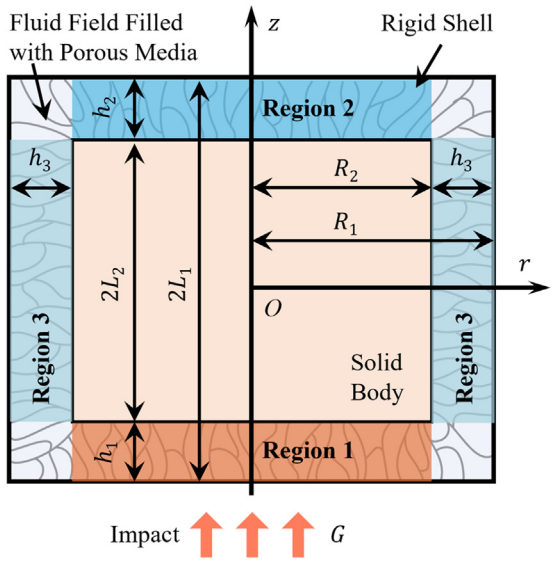

FIG. 2. Sketch of the theoretical model. The model represents the skull as a rigid cylindrical shell and the brain as a smaller solid cylinder at the center. The gap between them, simulating the SAS, is divided into three regions: region 1 (bottom) with thickness h_1, region 2 (top) with thickness h_2, and region 3 (side) with a constant thickness h_3. The acceleration of the outer shell, G, acts as a body force within the system. This cylindrical model allows for simplified analysis while capturing key structural features of the intracranial space.

However, this geometric simplification introduces certain limitations. It does not fully replicate the asymmetrical and irregular anatomical structure of the human skull, which may affect the accuracy of localized pressure responses and the distribution of forces across the intracranial cavity. Future studies could benefit from more anatomically detailed models to capture these complex interactions more accurately.

The coordinate system and geometrical dimensions are illustrated in Fig. 2. The radius and length of the outer container are R_1 and $2L_1$, respectively, while the radius and length of the solid inner object are R_2 and $2L_2$, respectively. We employ cylindrical coordinates with the radial r-axis and the vertical z-axis, with the origin fixed at the center of the outer container. Given the incompressibility of both the liquid and the solid inner object, the acceleration of the outer container is equivalent to a body force, valued at -G, acting within the inner space of the container.

The gap between the two cylinders can be divided into three regions: region 1, corresponding to the coup region in the head, with a thickness h_1 at the bottom; region 2, corresponding to the contrecoup region in the head, with a thickness h_2 at the top, and region 3, near the sidewall, with a thickness $h_3 = R_1 - R_2$. For the problem discussed herein, h_3 remains unchanged, while h_1 and h_2 vary over time. The pressure responses in these three regions are denoted as $P_{d,j}$, where $j = 1, 2, 3$ corresponds to regions 1, 2, and 3, respectively.

For the flow within region 1 and region 2, the presence of porous media introduces Darcy's effect, while the transient nature of the system highlights the importance of the inertial effect. Therefore, the Darcy–Lapwood–Brinkman equation is used to describe the fluid flow within these two regions, capturing the complex interplay of these factors,[71]

$$\frac{\partial \mathbf{u}}{\partial t} + (\mathbf{u}\cdot\nabla)\mathbf{u} = -\frac{1}{\rho}\nabla P + \nu\nabla^2\mathbf{u} - \frac{\nu}{K_p}\mathbf{u}, \tag{1}$$

where $\mathbf{u}$ represents the local macroscopic velocity, t is the time, ρ is the density, P denotes the pressure, ν is the kinematic viscosity, and K_p is the Darcy permeability. Due to the small gap thickness, the pressure gradient is negligible through the gap thickness, and hence, gravitational force has been neglected in this model. This simplification allows us to focus on the primary forces driving CSF flow and brain motion under impact conditions.

External impacts generate acceleration on the rigid shell, equivalent to applying a body force within the inner space. To demonstrate the roles of static pressure caused by the body force and dynamic pressure response caused by the flow, the following equation is defined:

$$P = -\rho z G + P_d(r,z), \tag{2}$$

where P_d is the dynamic pressure response caused by the squeezing flow. The first term on the right side represents the static pressure due to the body force.

As shown in Fig. 2, the flow is axisymmetric with no circumferential component, and therefore occurs only along the axial and radial directions. Consequently, the flow is only defined by its radial velocity, v_r, and vertical velocity, v_z. Then, Eq. (1) only contains the radial and vertical components,

$$\frac{\partial v_r}{\partial t} + v_r\frac{\partial v_r}{\partial r} + v_z\frac{\partial v_r}{\partial z} = -\frac{1}{\rho}\frac{\partial P_d}{\partial r} + \nu\left[\frac{\partial}{\partial r}\left(\frac{1}{r}\frac{\partial}{\partial r}(rv_r)\right) + \frac{\partial^2 v_r}{\partial z^2}\right] - \frac{\nu}{K_p}v_r, \tag{3}$$

$$\frac{\partial v_z}{\partial t} + v_r\frac{\partial v_z}{\partial r} + v_z\frac{\partial v_z}{\partial z} = -\frac{1}{\rho}\frac{\partial P_d}{\partial z} + \nu\left[\frac{1}{r}\frac{\partial}{\partial r}\left(r\frac{\partial v_z}{\partial r}\right) + \frac{\partial^2 v_z}{\partial z^2}\right] - \frac{\nu}{K_p}v_z. \tag{4}$$

The problem can be further defined using dimensionless numbers as follows: $\varepsilon = h/R$, $r^* = r/R$, $z^* = z/h$, $v_z^* = v_z/V_0$, $v_r^* = v_r/(V_0/\varepsilon)$, $P_d^* = P_d/(V_0\rho\nu R^2/h_0^3)$, $t^* = t/t_0$, $h^* = h/h_0$, Reynolds number, $\mathrm{Re} = V_0 h/(\nu\varepsilon)$, Womersley number, $\mathrm{Wo} = \sqrt{h^2/(t_0\nu)}$, and Brinkman number, $\mathrm{Br} = \sqrt{h^2/K_P}$, where V_0 is the characteristic velocity. With these definitions, Eqs. (3) and (4) can be reformulated into a dimensionless format, simplifying the analysis and highlighting the governing parameters of the system,

$$h^{*3}\frac{\partial P_d^*}{\partial r^*} = -\mathrm{W_o^2}\frac{\partial v_r^*}{\partial t^*} - \varepsilon\mathrm{Re}\left(v_r^*\frac{\partial v_r^*}{\partial r^*} + v_z^*\frac{\partial v_r^*}{\partial z^*}\right) + \varepsilon^2\frac{\partial}{\partial r^*}\left[\frac{1}{r^*}\frac{\partial}{\partial r^*}\left(r^* v_r^*\right)\right] + \frac{\partial^2 v_r^*}{\partial z^{*2}} - \mathrm{Br}^2 v_r^*, \tag{5}$$

$$h^{*3}\frac{\partial P_d^*}{\partial z^*} = \varepsilon^2\left\{-\mathrm{W_o^2}\frac{\partial v_z^*}{\partial t^*} - \varepsilon\mathrm{Re}\left(v_r^*\frac{\partial v_z^*}{\partial r^*} + v_z^*\frac{\partial v_z^*}{\partial z^*}\right) + \left[\varepsilon^2\frac{1}{r^*}\frac{\partial}{\partial r^*}\left(r^*\frac{\partial v_z^*}{\partial r^*}\right) + \frac{\partial^2 v_z^*}{\partial z^{*2}} - \mathrm{Br}^2 v_z^*\right]\right\}. \tag{6}$$

Given that the gap is very thin (i.e., $\varepsilon \ll 1$), Eqs. (5) and (6) imply that the vertical pressure gradient is negligible. Additionally, the convective terms and radial diffusive terms can be neglected due to the presence of a small coefficient, ε, which significantly reduces their contribution. Hence, P_d^* is only a function of radius and time, and Eqs. (5) and (6) can be simplified as

$$h^{*3}\frac{\partial P^*(r^*,t^*)}{\partial r^*} = -\mathrm{Wo}^2\frac{\partial v_r^*}{\partial t^*} + \frac{\partial^2 v_r^*}{\partial z^{*2}} - \mathrm{Br}^2 v_r^*. \tag{7}$$

Therefore, the corresponding dimensional governing equation in region 1 and region 2 can be written as

$$\frac{\partial v_r}{\partial t} = -\frac{1}{\rho}\frac{\partial P_{d,j}}{\partial r} + \nu\frac{\partial^2 v_r}{\partial z^2} - \frac{\nu}{K_p}v_r, \quad j = 1,2. \tag{8}$$

Applying no-slip and non-penetration boundary conditions at the boundary, according to our previous theoretical solution,[31,47] Eq. (8) can be analytically solved as

$$P_{d_j} = \frac{1}{2}\rho\left(R_2^2 - r^2\right)\left\{\left(\frac{dh_j}{dt}\right)^2\frac{1}{2h_j^2} - \frac{1}{2h_j}\frac{d^2h_j}{dt^2} - \nu\left[\frac{1}{4}\frac{dh_j}{dt}\frac{K_P^{-1.5}\cosh\left(K_P^{-0.5}\cdot\frac{h_j}{2}\right)}{\sinh\left(K_P^{-0.5}\cdot\frac{h_j}{2}\right) - \sqrt{\frac{1}{K_P}}\cdot\frac{h_j}{2}\cdot\cosh\left(K_P^{-0.5}\cdot\frac{h_j}{2}\right)} + \frac{1}{2}\frac{dh_j}{dt}\sum_{i=1}^{\infty}\exp\left[-\left(\frac{1}{K_P} + 4\frac{x_i^2}{h_j^2}\right)\nu t\right] \times \frac{-\left(2x_i/h_j\right)^3\cos(x_i)}{\left(\frac{h_j^2}{4K_P} + x_i^2\right)\sin(x_i)}\right]\right\} + D_j, \quad j = 1,2, \tag{9}$$

where x_i is the eigenvalue solved by $\tan(x_i) = x_i$, $i = 1, 2, \ldots, \infty$, and D_j is the pressure at the interface between region j and 3.

Region 3, as shown in Fig. 2, represents a porous channel with a constant gap. The porous media would average the flow within a short entrance region. Therefore, this study assumes the flow is unidirectional, and Darcy's law is applied to estimate the flow resistance in this region,

$$\frac{\partial P_{d,3}}{\partial z} = -\rho\frac{\nu}{K_p}\frac{Q_3}{\pi\left(R_1^2 - R_2^2\right)}, \tag{10}$$

where Q_3 is the flow rate of region 3. According to the mass conservation, Q_3 equals the flow rate leaving region 1, which has

$$Q_3 = -\pi R_2^2\frac{dh_1}{dt}. \tag{11}$$

Assuming $P_{d,3} = 0$ at $z = 0$, Eq. (10) can be solved as

$$P_{d,3} = \rho\frac{\nu}{K_p}\frac{R_2^2}{\left(R_1^2 - R_2^2\right)}\frac{dh_1}{dt}z. \tag{12}$$

Assuming $P_{d,1} = P_{d,3}$ at $r = R_2$, $z = -L_2$ and $P_{d,2} = P_{d,3}$ at $r = R_2$, $z = L_2$, one obtains

$$D_j = (-1)^j\rho\frac{\nu}{K_p}\frac{R_2^2}{\left(R_1^2 - R_2^2\right)}\frac{dh_1}{dt}L_2, \quad j = 1, 2. \tag{13}$$

The AT is a type of soft porous structure with fibers loosely tethered to the inner side of the skull and the outer side of the brain. Hence, it is

reasonable to assume, as a first approximation, that the solid structure of the AT does not exert any significant force on the motion of the brain. Applying Newton's second law to the inner solid object yields the governing equation,

$$m\frac{d^2s}{dt^2} = F_b + F_p. \tag{14}$$

Here, s represents the displacement of the inner object, and $m = 2\pi R_2^2 L_2 \rho_s$ is the mass of the inner object with ρ_s being its density. F_b denotes the total body force, and F_p represents the total force from pressure, which has the expression

$$F_b = -mG, \quad \text{and} \quad F_p = \int_A PdA, \tag{15}$$

where A indicates the total surface area of the inner solid object.

Substituting Eq. (2) in Eq. (14), it has

$$F_p = \int_A -\rho z G dA + \sum_{i=1}^{2}\int_{A_i} P_{d,i}dA_i, \tag{16}$$

where A_1 and A_2 represent the surface area of the inner object at regions 1 and 2, respectively.

Substituting Eqs. (9), (15), and (16) in Eq. (14), the governing equation about the inner solid object can be obtained as

$$\frac{d^2s}{dt^2} = \frac{-16\pi(\rho_s-\rho_l)GR^2L_2 + 2\pi\rho_l R_2^4(\gamma_1-\gamma_2) + 16\pi R_2(D_1-D_2)}{8m + \pi\rho R_2^4(1/h_1 + 1/h_2)}, \tag{17}$$

where

$$\gamma_j = \left(-\nu\left[\frac{1}{4}\frac{dh_j}{dt}\frac{K_P^{-1.5}\cosh\left(K_P^{-0.5}\cdot\frac{h_j}{2}\right)}{\sinh\left(K_P^{-0.5}\cdot\frac{h_j}{2}\right) - K_P^{-0.5}\cdot\frac{h_j}{2}\cdot\cosh\left(K_P^{-0.5}\cdot\frac{h_j}{2}\right)} + \frac{1}{2}\frac{dh_j}{dt}\sum_{i=1}^{\infty}\exp\left[-\left(\frac{1}{K_P}+4\frac{x_i^2}{h_j^2}\right)\nu t\right]\frac{-\left(\frac{2x_i}{h_j}\right)^3\cos(x_i)}{\left(\frac{h_j^2}{4K_P}+x_i^2\right)\sin(x_i)}\right] + \left(\frac{dh_j}{dt}\right)^2\frac{1}{2h_j^2}\right). \tag{18}$$

III. RESULTS AND DISCUSSION

This section presents the theoretical predictions for the investigated system, highlighting the significant influence of the porous AT. According to the parameters outlined in Eqs. (17) and (18), factors, such as the acceleration of the container, the gap thickness, the density of the inner object, and the permeability of the AT, affect the response of the system.

The density of brain matter ranges from 1.001 to 1.620 g/cm^3, which is higher than that of the CSF, ranging from 0.958 to 1.163 g/cm^3.[72] Theoretically, a greater density difference intensifies the response in the intracranial space. In this study, a representative density ratio $\rho_s/\rho_l = 1.1$ is choosen. The average gap thickness of the SAS is approximately 3 mm,[13] and the length scale of the head is about 150 mm. Consequently, a geometry ratio $\varepsilon = R_2/R_1 = L_2/L_1 = 0.96$ is used in the calculations.

Existing studies have determined the physical parameters of the SAS and AT. The health SAS has a porosity of 0.99.[73,74] The characteristics of AT, including its diameter and mechanical properties, have been observed to vary across different locations. Reported diameters range from 5 μm to below 100 μm.[19,75] In this study, three scenarios are considered in the results: healthy AT, damaged AT, and absence of AT. The AT is modeled as an evenly distributed fibrous medium with a fiber radius $R_f = 30$ μm. For the healthy AT scenario, the porosity is set to 0.99, while for the damaged AT scenario, the porosity is increased to 0.995. The permeability is calculated using the empirical equation developed by Zhu *et al.*,[69]

$$\frac{K_p}{R_f^2} = \frac{0.22 - 22.13\phi + 10.85\phi^2 + 11.00\phi^3 - 21.91(1-\phi)\ln(1-\phi)}{12(1-\phi)^2}. \tag{19}$$

Two types of external impacts, including constant acceleration and periodic acceleration, are adopted to investigate the response of the system. The inner solid object is assumed to be at the center of the shell with an initial gap thickness h_0.

Figure 3 presents the response of the SAS with AT (blue dot curve), SAS with damaged AT (purple dot-dash curve), and SAS without AT (red solid curve) under constant acceleration for one second, displaying the following variables: dimensionless displacement $s^* = s/h_0$, dimensionless acceleration $a_c^* = (d^2s/dt^2)/G$, the dimensionless pressure response at the center of region 1 $P_{d1c}^* = P_{d1}|_{r=0}/(\rho G L_2)$, and the dimensionless pressure response at the center of region 2 $P_{d2c}^* = (P_{d2}|_{r=0})/(\rho G L_2)$. These responses are presented in four rows, respectively. Three columns in the figure represent conditions with $G = 2g$, $4g$, $8g$, respectively.

Using dimensionless parameters provides a universal framework for interpreting the SAS response under different impact scenarios. The dimensionless displacement s^* reflects how the brain's position shifts as a proportion of the initial SAS gap height, highlighting relative motion instead of absolute distance. The dimensionless acceleration a_c^* expresses the brain's response to impact forces in terms of relative acceleration, facilitating comparisons across different gravitational loadings. Dimensionless pressure responses P_{d1c}^* and P_{d2c}^* indicate the normalized dynamic pressure at the center of regions 1 and 2, respectively, scaled by the static pressure caused by the body force. For instance, the dimensionless peak value of P_{d1c}^* under $G = 2g$ shown in Fig. 3 is 0.66, corresponding to a pressure response of 1.861 kPa.

For example, the dimensionless peak value of P_{d1c}^* under $G = 2g$ shown in Fig. 3 is 0.66, representing a pressure response of 1.861 kPa.

Figure 3 shows that once constant acceleration is applied to the rigid shell, s^* starts to decrease. With a higher acceleration, the inner solid object moves downward much faster. Importantly, the presence of porous media significantly slows down the displacement, indicating that the porous media can stabilize the movement of the inner solid object.

Correspondingly, Fig. 3 shows that a_c^* begins with a negative value and then increases to a positive value to counteract the downward motion. A peak positive acceleration is observed in the absence of porous media, while there is almost no positive pressure response with porous media. The duration of the positive acceleration is much

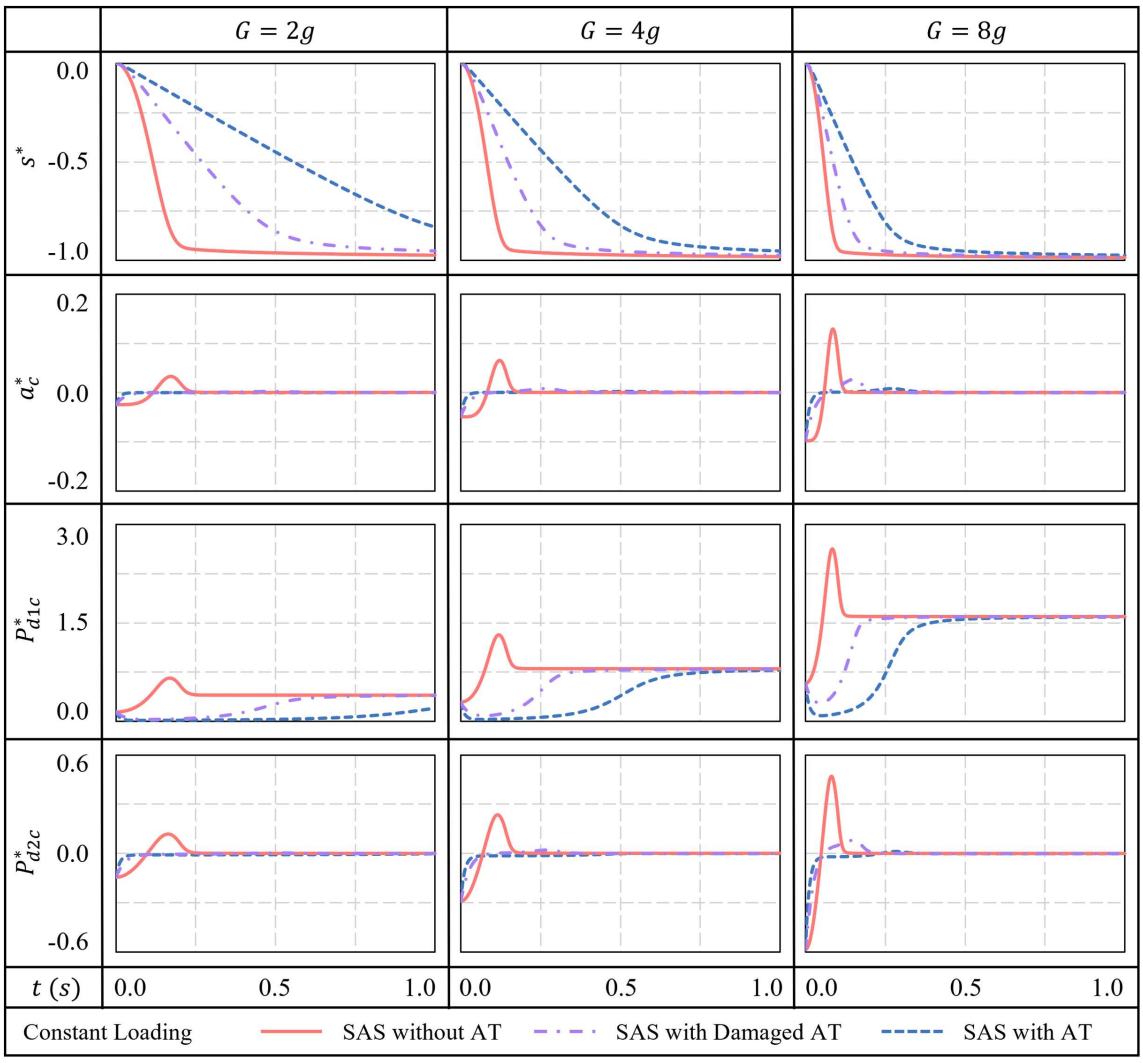

FIG. 3. Response of the SAS with AT, with damaged AT, and without AT under constant acceleration. The results include the dimensionless displacement s^*, dimensionless acceleration a_c^*, and the dimensionless pressure responses at the center of region 1 (P_{d1c}^*) and region 2 (P_{d2c}^*). The rows correspond to these parameters, respectively, while the columns represent different acceleration conditions ($G = 2g$, $4g$, $8g$). The solid red curve represents the condition with a pure fluid gap, and the dotted blue curve represents the condition with porous media.

longer and more severe in the absence of porous media conditions. Higher accelerations result in greater magnitudes of both positive and negative peak accelerations.

Similarly, the presence of porous media significantly reduces the pressure response within the SAS. In Fig. 3, P_{d1c}^* represents the pressure response in the bottom region, indicating a positive pressure response. Under conditions without porous media, P_{d1c}^* quickly rises to a peak and then decreases to a value that ensures the inner object moves with the rigid shell. Conversely, for conditions with porous media, P_{d1c}^* initially follows a similar pressure response to overcome the inertia of the fluid in the gap. Subsequently, P_{d1c}^* gradually increases to match the value of P_{d1c}^* observed in the nonporous media condition. Although more resistance is encountered as the fluid is squeezed out of the porous region, facilitating pore pressure generation, the motion and acceleration of the inner object are much slower. Consequently, the squeezing velocity is much lower, reducing pressure generation. Overall, the latter effect is more pronounced, resulting in a slower pressure response without any overshoot when porous media is present.

Figure 3 also shows the response of P_{d2c}^*, the pressure response in the top region. The pressure in this region is negative because it is initially an expanding flow when the impact occurs. The magnitude of P_{d2c}^* is much smaller than that of P_{d1c}^* because the gap thickness increases during the expanding process. The general behavior of P_{d2c}^* is similar to that of a_c^*. In the absence of porous media conditions, P_{d2c}^* increases from a negative value to a positive peak and then decreases to zero. In the presence of porous media, P_{d2c}^* starts from the same

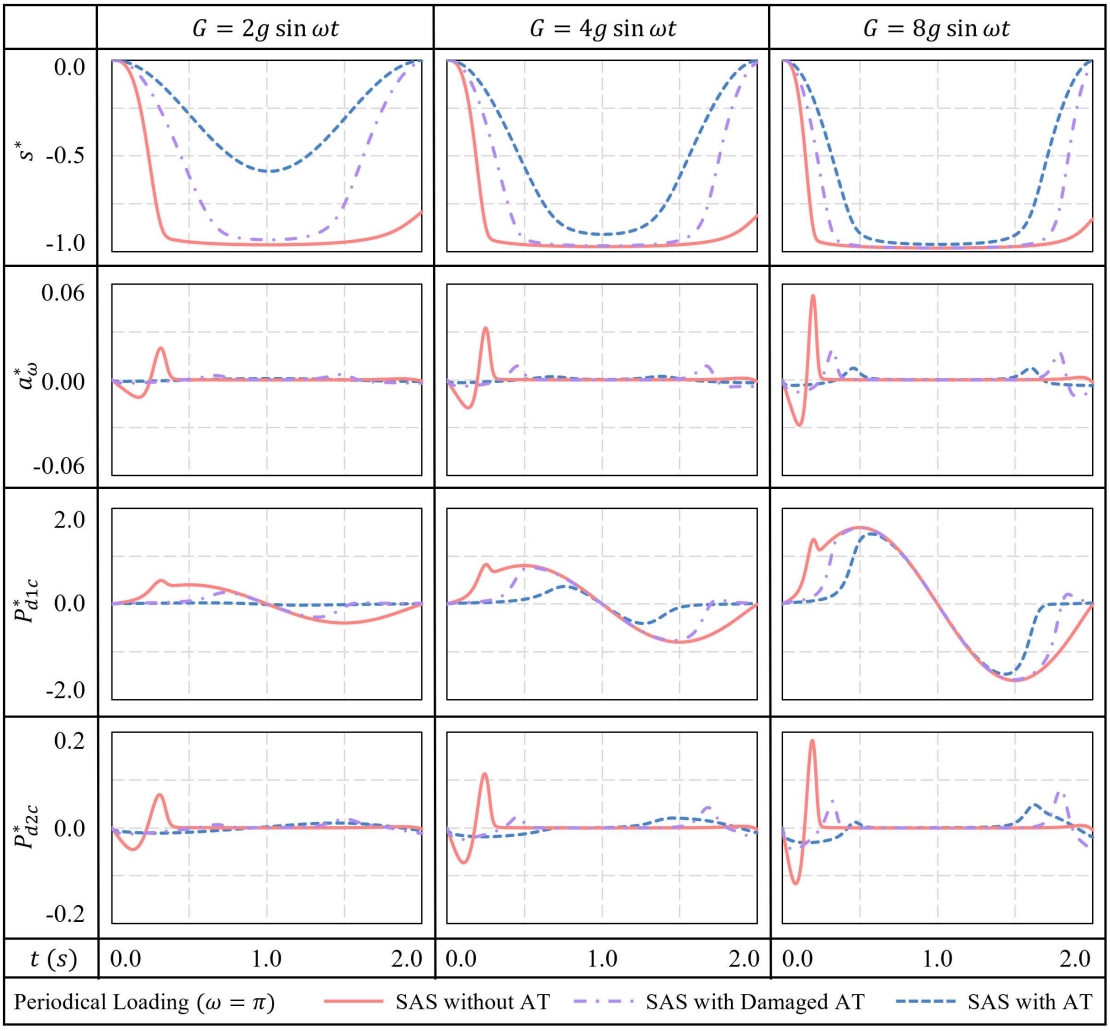

FIG. 4. Response of the SAS with AT, with damaged AT, and without AT under lower frequency periodic acceleration ($G = A\sin\omega t$) within two seconds ($\omega = \pi$). The results include the dimensionless displacement s^*, dimensionless acceleration a^*_ω, and the dimensionless pressure responses at the center of region 1 (P^*_{d1c}) and region 2 (P^*_{d2c}). The rows correspond to these parameters, respectively, while the columns represent different acceleration conditions ($A = 2g,\ 4g,\ 8g$). The solid red curve represents the condition with a pure fluid gap, and the dotted blue curve represents the condition with porous media.

negative value and quickly rises to nearly zero due to the significantly increased damping effect.

Overall, Fig. 3 highlights the response of the system to constant acceleration, emphasizing the critical role of porous media in stabilizing intracranial dynamics. When acceleration is applied, the inner solid object moves downward, but porous media significantly dampens this displacement, reducing peak accelerations. The pressure responses in different regions show that porous media modulates pressure, preventing extreme peaks seen in nonporous conditions. The fundamental mechanism involves the interplay of fluid inertia, viscous forces, and porous resistance, underscoring the importance of porous media in mitigating dynamic intracranial responses.

Figures 4 and 5 present the response of the SAS with AT (blue dot curve), SAS with damaged AT (purple dot-dash curve), and SAS without AT (red solid curve) under periodic acceleration over a duration of two seconds, displaying the same four variables shown in Fig. 3: dimensionless displacement s^*, dimensionless acceleration a^*_ω, and the dimensionless pressure responses P^*_{d1c} and P^*_{d2c}. The periodic acceleration condition defines $a^*_\omega = (d^2s/dt^2)/A$. The acceleration of the rigid shell is given by $G = A\sin\omega t$, where A is the amplitude and ω is the angular frequency in Fig. 4, $\omega = \pi$, and in Fig. 5, $\omega = 2\pi$. Three columns in Figs. 4 and 5 correspond to conditions with $A = 2g,\ 4g,\ 8g$, respectively.

Figure 4, with a frequency of 0.5 Hz, demonstrates that for pure fluid gap conditions, the dimensionless displacement s^* initially decreases to a relatively small value, similar to the behavior shown in Fig. 3, and then slightly increases in the later stages. In contrast, for the condition with porous media, s^* follows the same periodic pattern as the acceleration. It decreases to a negative value with a smaller magnitude and returns to the origin point at the end of each period, highlighting the damping effect of the porous media.

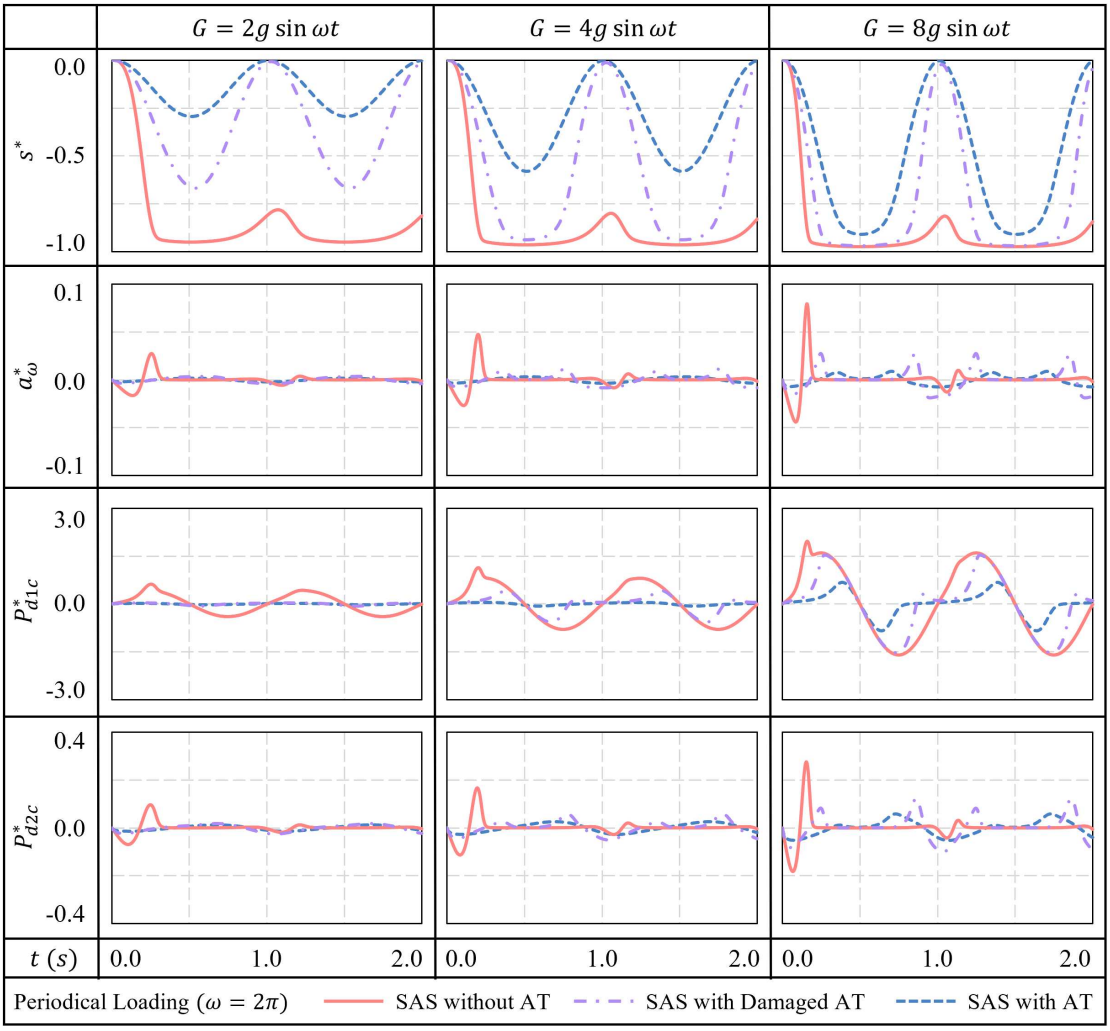

FIG. 5. Response of the SAS with AT, with damaged AT, and without AT under higher frequency periodic acceleration ($G = A\sin\omega t$) within two seconds ($\omega = 2\pi$). The results include the dimensionless displacement s^*, dimensionless acceleration a^*_ω, and the dimensionless pressure responses at the center of region 1 (P^*_{d1c}) and region 2 (P^*_{d2c}). The rows correspond to these parameters, respectively, while the columns represent different acceleration conditions ($A = 2g$, $4g$, $8g$). The solid red curve represents the condition with a pure fluid gap, and the dotted blue curve represents the condition with porous media.

Figure 4 indicates a^*_ω for the pure fluid gap condition varies primarily at the starting state, first decreasing to a negative peak, then increasing to a positive peak, and finally decreasing to nearly zero. Conversely, a^*_ω for the porous media condition exhibits an excellent damping effect, maintaining a nearly zero response throughout the period.

Figure 4 shows that P^*_{d1c} for the pure fluid gap condition follows the same trend as the periodic acceleration. There is a small peak when a^*_ω reaches its maximum value caused by the rapidly decreasing gap thickness. As the amplitude increases, the variation of P^*_{d1c} also increases. In contrast, P^*_{d1c} for the porous media condition is much more subdued. When $A = 2g$, the variation is negligible. For $A = 4g$ and $8g$, both the peak value and duration of P^*_{d1c} are significantly less severe than in the pure fluid gap condition.

Similar to the phenomenon observed in Fig. 3, due to the larger gap thickness in the top region, P^*_{d2c} exhibits a smaller magnitude compared to P^*_{d1c}. Additionally, the trend of P^*_{d2c} closely mirrors that of a^*_ω. The variation in P^*_{d2c} for the porous media condition is significantly smaller compared to the pure fluid gap condition, demonstrating the damping effect of the porous media.

Figure 4 demonstrates that porous media significantly stabilizes the system's response under periodic acceleration. The porous media condition results in less pronounced displacement, acceleration, and pressure variations, highlighting its effective damping capability. The pure fluid condition exhibits more extreme variations, particularly at higher acceleration magnitudes.

Figure 5 presents the system response at a higher frequency ($\omega = 2\pi$) compared to the results shown in Fig. 4 ($\omega = \pi$). With the amplitude remaining the same, a higher frequency results in faster motion and greater acceleration. Consequently, the acceleration and pressure responses are generally higher than the results shown in

Fig. 4. However, due to the more rapid changes in the acceleration direction, the inner solid object has less time to accelerate, leading to smaller displacements than those observed in Fig. 4.

Overall, the trends in Fig. 5 are similar to those observed in Fig. 4. Additionally, the results in Fig. 5 highlight the increased stability provided by the porous media under higher frequency periodic acceleration, further stabilizing the system's response and reducing variations in displacement, acceleration, and pressure.

The findings of the above-mentioned results have significant implications for understanding and mitigating brain injuries. The brain is subjected to various accelerative forces in real-world applications, such as those experienced during sports impacts, vehicular accidents, or falls. The presence of porous media, analogous to the AT in the SAS, plays a crucial role in stabilizing intracranial dynamics. The results demonstrate that porous media effectively dampens displacement, acceleration, and pressure variations, reducing the severity of brain movement and the associated risk of injury. This damping effect is significant under higher frequency impacts, which are common in real-world scenarios.

IV. CONCLUSION

In this paper, we developed a simplified theoretical model, based on critical physical insights, to provide the first investigation of CSF flow in the highly porous AT network within the SAS and the resulting motion of brain matter when the head is exposed to a sudden external impact. It highlights the crucial role of AT in stabilizing intracranial dynamics under external impacts. Key findings include the significant damping effect of porous media, which reduces displacement, acceleration, and pressure variations. This stabilization is significant under higher frequency periodic accelerations, where porous media effectively mitigate the severity of brain movement and associated pressure changes.

While the model developed in this study provides valuable physical insights, it is important to acknowledge the simplification of assuming a constant gap thickness in the SAS. This assumption facilitates analytical tractability by reducing model complexity, yet it does not fully capture the anatomical variations in gap thickness that may arise from the brain's uneven surface and impact dynamics. Future research could extend this model by incorporating a variable gap thickness to improve physiological accuracy, particularly in experimental or computational studies aimed at achieving closer alignment with real-world head impacts. Such modifications would enable a more precise assessment of intracranial pressure variations and brain displacement, further enhancing our understanding of CSF flow and brain stabilization mechanisms under diverse impact scenarios.

It is noted that we did not take into account the compression/stretch of the AT, given its very soft structure, and only considered the interaction between the CSF and the brain matter. If one includes the solid phase reaction force arising from the compression/extension of the AT, the restrictive and protective effects would be even stronger. On the other hand, if the AT network is impaired, as occurs in diseases like Alzheimer's disease,[76–78] the patient would be more sensitive to head impacts and more likely to suffer from concussive brain injury compared to healthy subjects when exposed to the same level of impact.

This paper contributes to uncovering the mystery of brain concussions. It also sheds light on the development of biomimetic porous materials that replicate the damping effect of the AT, providing a promising strategy for protecting the brain from traumatic injuries. This approach could inform the design of protective headgear, medical treatments, and safety protocols to minimize the impact of sudden accelerative forces on the brain.

ACKNOWLEDGMENTS

J. Lang acknowledges the support from the National Natural Science Foundation of China (No. 12202101) and the Natural Science Foundation of Jiangsu Province (No. BK20220793). Q. Wu acknowledges the support from the National Science Foundation (No. 2322067).

AUTHOR DECLARATIONS

Conflict of Interest

The authors have no conflicts to disclose.

Author Contributions

Ji Lang: Conceptualization (equal); Data curation (lead); Methodology (lead); Writing – original draft (lead). **Qianhong Wu:** Conceptualization (equal); Validation (lead); Writing – review & editing (lead).

DATA AVAILABILITY

The data that support the findings of this study are available from the corresponding author upon reasonable request.

REFERENCES

[1]Centers for Disease Control and Prevention, "Sports-related recurrent brain injuries—United States," Morb. Mortal. Wkly. Rep. **46**, 224 (1997).
[2]D. J. Thurman, C. M. Branche, and J. E. Sniezek, "The epidemiology of sports-related traumatic brain injuries in the United States: Recent developments," J. Head Trauma Rehabil. **13**, 1 (1998).
[3]J. Lang, R. Nathan, and Q. Wu, "How to deform an egg yolk? On the study of soft matter deformation in a liquid environment," Phys. Fluids **33**, 011903 (2021).
[4]S. H. Rauchman, A. Zubair, B. Jacob, D. Rauchman, A. Pinkhasov, D. G. Placantonakis, and A. B. Reiss, "Traumatic brain injury: Mechanisms, manifestations, and visual sequelae," Front. Neurosci. **17**, 1 (2023).
[5]M. Faul, L. Xu, M. M. Wald, and V. G. Coronado, "Traumatic brain injury in the United States; Emergency department visits, hospitalizations, and deaths, 2002–2006" (Centers for Disease Control and Prevention National Center for Injury Prevention and Control, 2010).
[6]M. W. Collins, G. L. Iverson, M. R. Lovell, D. B. McKeag, J. Norwig, and J. Maroon, "On-field predictors of neuropsychological and symptom deficit following sports-related concussion," Clin. J. Sport Med. **13**, 222 (2003).
[7]J. A. Langlois, W. Rutland-Brown, and M. M. Wald, "The epidemiology and impact of traumatic brain injury: A brief overview," J. Head Trauma Rehabil. **21**, 375 (2006).
[8]M. R. Schulz, S. W. Marshall, F. O. Mueller, J. Yang, N. L. Weaver, W. D. Kalsbeek, and J. M. Bowling, "Incidence and risk factors for concussion in high school athletes, North Carolina, 1996–1999," Am. J. Epidemiol. **160**, 937 (2004).
[9]H. S. Levin and R. R. Diaz-Arrastia, "Diagnosis, prognosis, and clinical management of mild traumatic brain injury," Lancet Neurol. **14**, 506 (2015).
[10]V. Pavlov, P. Thompson-Leduc, L. Zimmer, J. Wen, J. Shea, H. Beyhaghi, S. Toback, N. Kirson, and M. Miller, "Mild traumatic brain injury in the United States: Demographics, brain imaging procedures, health-care utilization and costs," Brain Inj. **33**, 1151 (2019).

[11]P. McMahon *et al.*, "Symptomatology and functional outcome in mild traumatic brain injury: Results from the prospective TRACK-TBI study," J. Neurotrauma **31**, 26 (2014).
[12]L. Ganti, T. Stead, Y. Daneshvar, A. N. Bodhit, C. Pulvino, S. W. Ayala, and K. R. Peters, "GCS 15: When mild TBI isn't so mild," Neurol. Res. Pract. **1**, 6 (2019).
[13]P. Saboori and A. Sadegh, "Material modeling of the head's subarachnoid space," Sci. Iran. **18**, 1492 (2011).
[14]M. Sotudeh Chafi, G. Karami, and M. Ziejewski, "Simulation of blast-head interactions to study traumatic brain injury," in *Volume 2: Biomedical and Biotechnology Engineering* (ASME, 2007), pp. 211–220.
[15]W. C. Moss, M. J. King, and E. G. Blackman, "Skull flexure from blast waves: A mechanism for brain injury with implications for helmet design," Phys. Rev. Lett. **103**, 108702 (2009).
[16]N. Benko, E. Luke, Y. Alsanea, and B. Coats, "Mechanical characterization of the human pia-arachnoid complex," J. Mech. Behav. Biomed. Mater. **120**, 104579 (2021).
[17]G. Fabris, Z. M. Suar, and M. Kurt, "Micromechanical heterogeneity of the rat pia-arachnoid complex," Acta Biomater. **100**, 29 (2019).
[18]N. Benko, E. Luke, Y. Alsanea, and B. Coats, "Spatial distribution of human arachnoid trabeculae," J. Anat. **237**, 275 (2020).
[19]H. E. Killer, H. R. Laeng, J. Flammer, and P. Groscurth, "Architecture of arachnoid trabeculae, pillars, and septa in the subarachnoid space of the human optic nerve: Anatomy and clinical considerations," Br. J. Ophthalmol. **87**, 777 (2003).
[20]S. Gupta, M. Soellinger, D. M. Grzybowski, P. Boesiger, J. Biddiscombe, D. Poulikakos, and V. Kurtcuoglu, "Cerebrospinal fluid dynamics in the human cranial subarachnoid space: An overlooked mediator of cerebral disease. I. Computational model," J. R Soc. Interface **7**, 1195 (2010).
[21]M. Olczak, ŁA. Poniatowski, A. Siwińska, and M. Kwiatkowska, "Post-mortem detection of neuronal and astroglial biochemical markers in serum and urine for diagnostics of traumatic brain injury," Int. J. Legal Med. **137**, 1441 (2023).
[22]M. R. Grovola, C. von Reyn, D. J. Loane, and D. K. Cullen, "Understanding microglial responses in large animal models of traumatic brain injury: An underutilized resource for preclinical and translational research," J. Neuroinflammation **20**, 67 (2023).
[23]J. Lang, R. Nathan, D. Zhou, X. Zhang, B. Li, and Q. Wu, "Cavitation causes brain injury," Phys. Fluids **33**, 031908 (2021).
[24]A. Koster and A. Adnan, "Dynamic similitude of human head surrogates," Multiscale Sci. Eng. **6**, 179 (2024).
[25]Y. Li, P. Vakiel, K. Adanty, S. Ouellet, A. H. Vette, D. Raboud, and C. R. Dennison, "Influence of surrogate scalp material and thickness on head impact responses: Toward a biofidelic head-brain physical model," J. Mech. Behav. Biomed. Mater. **142**, 105859 (2023).
[26]S. O. Linge, V. Haughton, A. E. Løvgren, K. A. Mardal, and H. P. Langtangen, "CSF flow dynamics at the craniovertebral junction studied with an idealized model of the subarachnoid space and computational flow analysis," Am. J. Neuroradiol. **31**, 185 (2010).
[27]U. Kertzscher, T. Schneider, L. Goubergrits, K. Affeld, D. Hänggi, and A. Spuler, "In vitro study of cerebrospinal fluid dynamics in a shaken basal cistern after experimental subarachnoid hemorrhage," PLoS One **7**, e41677 (2012).
[28]P. L. H. Chong, D. Garic, M. D. Shen, I. Lundgaard, and A. J. Schwichtenberg, "Sleep, cerebrospinal fluid, and the glymphatic system: A systematic review, sleep" Med. Rev. **61**, 101572 (2022).
[29]J. Lang, S. Santhanam, and Q. Wu, "Exact and approximate solutions for transient squeezing flow," Phys. Fluids **29**, 103606 (2017).
[30]J. Lang, L. Wang, and Q. Wu, "Theoretical study of oscillating squeezing flow through a porous medium," Tribol. Int. **162**, 107110 (2021).
[31]J. Lang, R. Nathan, and Q. Wu, "Theoretical and experimental study of transient squeezing flow in a highly porous film," Tribol. Int. **135**, 259 (2019).
[32]J. Stefan, "Versuche über die scheinbare adhäsion," Ann. Phys. **230**, 316 (1875).
[33]P. J. Leider and R. B. Bird, "Squeezing flow between parallel disks. I. Theoretical analysis," Ind. Eng. Chem. Fundam. **13**, 336 (1974).
[34]H. M. Laun, M. Rady, and O. Hassager, "Analytical Solutions for Squeeze Flow with Partial Wall Slip," J. Nonnewton. Fluid Mech. **81**, 1 (1999).
[35]R. Scheidl and C. Gradl, "An approximate computational method for the fluid stiction problem of two separating parallel plates with cavitation," J. Fluids Eng. **138**, 61301 (2016).
[36]D. B. Roemer, P. Johansen, H. C. Pedersen, and T. O. Andersen, "Fluid stiction modeling for quickly separating plates considering the liquid tensile strength," J. Fluids Eng. **137**, 61205 (2015).
[37]J. L. Livesey, "Inertia effects in viscous flows," Int. J. Mech. Sci. **1**, 84 (1960).
[38]J. D. Jackson, "A study of squeezing flow," Appl. Sci. Res. Sect. A **11**, 148 (1963).
[39]C. J. Lawrence, Y. Kuang, and S. Weinbaum, "The inertial draining of a thin fluid layer between parallel plates with a constant normal force. Part 2. Boundary layer and exact numerical solutions," J. Fluid Mech. **156**, 479 (1985).
[40]S. Weinbaum, C. J. Lawrence, and Y. Kuang, "The inertial draining of a thin fluid layer between parallel plates with a constant normal force. Part 1. Analytic solutions; inviscid and small-but finite-Reynolds-number limits," J. Fluid Mech. **156**, 463 (1985).
[41]J. Lang, R. Nathan, and Q. Wu, "Experimental study of transient squeezing film flow," J. Fluids Eng. **141**, 081110 (2019).
[42]C.-Y. Wang, "The squeezing of a fluid between two plates," J. Appl. Mech. **43**, 579 (1976).
[43]E. A. Moss, A. Krassnokutski, B. W. Skews, and R. T. Paton, "Highly transient squeeze-film flows," J. Fluid Mech. **671**, 384 (2011).
[44]T. Hayat, A. Qayyum, and A. Alsaedi, "MHD Unsteady Squeezing Flow over a Porous Stretching Plate," Eur. Phys. J. Plus **128**, 157 (2013).
[45]S. Ishizawa, "The unsteady laminar flow between two parallel discs with arbitrarily varying gap width," Bull. JSME **9**, 533 (1966).
[46]S.-M. Yang and L. G. Leal, "Thin fluid film squeezed with inertia between two parallel plane surfaces," J. Tribol. **115**, 632 (1993).
[47]J. Lang and Q. Wu, "Modeling of the transient cerebrospinal fluid flow under external impacts," Eur. J. Mech. - B/Fluids **87**, 171 (2021).
[48]A. I. King, J. S. Ruan, C. Zhou, W. N. Hardy, and T. B. Khalil, "Recent advances in biomechanics of brain injury research: A review," J. Neurotrauma **12**, 651 (1995).
[49]W. N. Hardy, C. D. Foster, A. I. King, and S. Tashman, "Investigation of brain injury kinematics: Introduction of a new technique," ASME Appl. Mech. Div. **225**, 241 (1997).
[50]P. Saboori, C. Germanier, and A. Sadegh, "Mechanics of CSF Flow through trabecular architecture in the brain," in *26th Southern Biomedical Engineering Conference SBEC 2010, April 30-May 2, 2010*, College Park, Maryland (Springer, 2010), pp. 440–443.
[51]G. A. Ateshian, "The role of interstitial fluid pressurization in articular cartilage lubrication," J. Biomech. **42**, 1163 (2009).
[52]Q. Wu, Y. Andreopoulos, S. Xanthos, and S. Weinbaum, "Dynamic compression of highly compressible porous media with application to snow compaction," J. Fluid Mech. **542**, 281 (2005).
[53]Q. Wu, S. Santhanam, R. Nathan, and Q. Wang, "A biphasic approach for the study of lift generation in soft porous media," Phys. Fluids **29**, 043602 (2017).
[54]Q. Wu, Y. Igci, Y. Andreopoulos, and S. Weinbaum, "Lift mechanics of downhill skiing and snowboarding," Med. Sci. Sports Exerc. **38**, 1132 (2006).
[55]T. Gacka, Z. Zhu, R. Crawford, R. Nathan, and Q. Wu, "From red cells to soft lubrication, an experimental study of lift generation inside a compressible porous layer," J. Fluid Mech. **818**, 5 (2017).
[56]Z. Zhu, R. Nathan, and Q. Wu, "An experimental study of the lubrication theory for highly compressible porous media, with and without lateral leakage," Tribol. Int. **127**, 324 (2018).
[57]J. Feng and S. Weinbaum, "Lubrication theory in highly compressible porous media: The mechanics of skiing, from red cells to humans," J. Fluid Mech. **422**, 281 (2000).
[58]Q. Wu, Y. Andreopoulos, and S. Weinbaum, "From red cells to snowboarding: A new concept for a train track," Phys. Rev. Lett. **93**, 194501 (2004).
[59]Q. Wu, Y. Andreopoulos, and S. Weinbaum, "Lessons learned from the exquisite design of the endothelial surface glycocalyx and their amazing applications," WIT Trans. Ecol. Environ. **73**, 1 (2004).
[60]R. Crawford, R. Nathan, L. Wang, and Q. Wu, "Experimental study on the lift generation inside a random synthetic porous layer under rapid compaction," Exp. Therm. Fluid Sci. **36**, 205 (2012).
[61]Q. Wu and Q. Sun, "A comprehensive skiing mechanics theory with implications to snowboard optimization," Med. Sci. Sports Exerc. **43**, 1955 (2011).
[62]B. Barabadi, R. Nathan, K. Jen, and Q. Wu, "On the characterization of lifting forces during the rapid compaction of deformable porous media," J. Heat Transfer **131**, 101006 (2021).

[63]H. Wu, "Squeeze-film behavior for porous annular disks," j. Lubr. Technol. **92**, 593 (1970).
[64]N. B. Naduvinamani, P. S. Hiremath, and G. Gurubasavaraj, "Squeeze film lubrication of a short porous journal bearing with couple stress fluids," Tribol. Int. **34**, 739 (2001).
[65]T. Karmakar and G. P. Raja Sekhar, "Squeeze-film flow between a flat impermeable bearing and an anisotropic porous bed," Phys. Fluids **30**, 043604 (2018).
[66]H. C. Brinkman, "A calculation of the viscous force exerted by a flowing fluid on a dense swarm of particles, flow," Turbul. Combust. **1**, 27 (1949).
[67]S. Whitaker, "Flow in porous media I: A theoretical derivation of Darcy's law," Transp. Porous Media **1**, 3 (1986).
[68]Q. Wu, S. Weinbaum, and Y. Andreopoulos, "Stagnation-point flows in a porous medium," Chem. Eng. Sci. **60**, 123 (2005).
[69]Z. Zhu, Q. Wang, and Q. Wu, "On the examination of the darcy permeability of soft fibrous porous media; new correlations," Chem. Eng. Sci. **173**, 525 (2017).
[70]R. Crawford, G. F. Jones, L. You, and Q. Wu, "Compression-dependent permeability measurement for random soft porous media and its implications to lift generation," Chem. Eng. Sci. **66**, 294 (2011).
[71]M. H. Hamdan, "Single-phase flow through porous channels a review of flow models and channel entry conditions," Appl. Math. Comput. **62**, 203 (1994).
[72]T. W. Barber, J. A. Brockway, and L. S. Higgins, "The density of tissues in and about the head," Acta Neurol. Scand. **46**, 85 (1970).
[73]A. F. Frydrychowski, A. Szarmach, B. Czaplewski, and P. J. Winklewski, "Subarachnoid space: New tricks by an old dog," PLoS One **7**, e37529 (2012).
[74]Y. Watanabe, S. Abe, K. Takagi, T. Yamamoto, and T. Kato, "Evolution of subarachnoid space in normal fetuses using magnetic resonance imaging," Prenat. Diagn. **25**, 1217 (2005).
[75]M. M. Mortazavi *et al.*, "Subarachnoid trabeculae: A comprehensive review of their embryology, histology, morphology, and surgical significance," World Neurosurg. **111**, 279 (2018).
[76]E. Mori, N. Hirono, H. Yamashita, T. Imamura, Y. Ikejiri, M. Ikeda, H. Kitagaki, T. Shimomura, and Y. Yoneda, "Premorbid brain size as a determinant of reserve capacity against intellectual decline in Alzheimer's disease," Am. J. Psychiatry **154**, 18 (1997).
[77]C. Decarli, P. Maillard, M. P. Pase, A. S. Beiser, D. Kojis, C. L. Satizabal, J. J. Himali, H. J. Aparicio, E. Fletcher, and S. Seshadri, "Trends in intracranial and cerebral volumes of Framingham heart study participants born 1930 to 1970," JAMA Neurol. **95817**, 471 (2024).
[78]Y. Chen, Y. Wang, Z. Song, Y. Fan, T. Gao, and X. Tang, "Abnormal white matter changes in Alzheimer's disease based on diffusion tensor imaging: A systematic review," Ageing Res. Rev. **87**, 101911 (2023).